nature communications

Article

https://doi.org/10.1038/s41467-024-54203-3

Designing giant Hall response in layered topological semimetals

Received: 28 February 2024

Accepted: 31 October 2024

Published online: 22 November 2024

Check for updates

Grigorii Skorupskii[1], Fabio Orlandi[2], Iñigo Robredo[3,8], Milena Jovanovic[1,4], Rinsuke Yamada[5], Fatmagül Katmer[1], Maia G. Vergniory[3,6], Pascal Manuel[2], Max Hirschberger[5,7] & Leslie M. Schoop[1]

Noncoplanar magnets are excellent candidates for spintronics. However, such materials are difficult to find, and even more so to intentionally design. Here, we report a chemical design strategy that allows us to find a series of noncoplanar magnets—Ln_3Sn_7 (Ln = Dy, Tb)—by targeting layered materials that have decoupled magnetic sublattices with dissimilar single-ion anisotropies and combining those with a square-net topological semimetal sublattice. Ln_3Sn_7 shows high carrier mobilities upwards of 17,000 $cm^2 \cdot V^{-1} \cdot s^{-1}$, and hosts noncoplanar magnetic order. This results in a giant Hall response with an anomalous Hall angle of 0.17 and Hall conductivity of over 42,000 $\Omega^{-1} \cdot cm^{-1}$—a value over an order of magnitude larger than the established benchmarks in $Co_3Sn_2S_2$ and Fe thin films.

Long-range ordered structures of magnetic moments that are neither parallel nor antiparallel, such as spin spirals, vortices, or hedgehogs, are a bridge, or compromise, between ferromagnets and antiferromagnets. These noncollinear magnets can have ferroic responses (e.g., spontaneous Hall effects) in the absence of a large net magnetization, avoiding slowing down dynamics or the creation of inconvenient stray fields. As such, these magnets have recently been invoked[1–4] in prospective data storage solutions which promise to eliminate many issues inherent in transistor-based technologies, including high power consumption and poor remanence, while also drastically improving access rates that are typically thought to be the Achilles' heel of magnetic memories.

Particularly viable are materials where the noncollinear magnetic order elicits a clear electrical transport response (e.g., in the Hall effect)[1,2], enabling easy interfacing with electronic devices. Recent work focuses on lattices of particle-like magnetic skyrmions, where the noncoplanar spin arrangement provokes topological Hall effect (THE)[5–7], which is sharply contained to the skyrmion lattice phase. Including skyrmion lattices, only a few dozen materials are known to host sharp Hall anomalies arising from magnetic order—for instance, chiral antiferromagnets $CoNb_3S_6$[8] and Mn_3Sn[9].

In some magnets with Hall anomalies, including Mn_3Sn, the strength of the anomaly is thought to originate in its nontrivial electronic topology: Mn_3Sn is a Weyl semimetal, and this electronic state produces a large Berry curvature that is responsible for the anomalous Hall effect[9,10]. These rare materials that combine topological semimetal (TSM) states with noncollinear magnetic structures are also interesting beyond the Hall effect anomalies: fundamentally, the interplay of the exotic physical phenomena arising from the nontrivial topology with noncollinear magnetism is not well studied or understood[11]. Beyond the fundamental interest, topological electronic states often result in high carrier mobilities, which can reduce resistive losses in devices. Altogether, there is a clear need to develop new materials that combine noncollinear magnetism with nontrivial topological states, which could produce both strong electrical transport signatures of magnetism, and high carrier mobilities.

Here, we report a series of such materials, alongside a chemical design strategy that allowed us to identify them. Our strategy is based

[1]Department of Chemistry, Princeton University, Princeton 08540 NJ, USA. [2]ISIS Neutron and Muon Source, STFC Rutherford Appleton Laboratory, Didcot OX11 0QX Oxfordshire, UK. [3]Donostia International Physics Center, Donostia-San Sebastian 20018 Gipuzkoa, Spain. [4]Department of Chemistry, North Carolina State University, Raleigh 27695 NC, USA. [5]Department of Applied Physics and Quantum-Phase Electronics Center (QPEC), The University of Tokyo, Bunkyo-ku, Tokyo 113-8656, Japan. [6]Département de physique et Institut quantique, Université de Sherbrooke, Sherbrooke J1K 2R1 QC, Canada. [7]RIKEN Center for Emergent Matter Science (CEMS), Wako, Saitama 351-0198, Japan. [8]Present address: Luxembourg Institute of Science and Technology (LIST), Avenue des Hauts-Fourneaux 5, L-4362 Esch/Alzette, Luxembourg. e-mail: lschoop@princeton.edu

on three key elements: (1) taking a layered magnetic system, where the layers are sufficiently decoupled to be considered separately; (2) ensuring the layers contain sublattices with dissimilar magnetic anisotropies, in order to produce noncoplanar texture from two coplanar building blocks or make an already noncoplanar structure even more complex (Fig. 1a); and (3) combining them with a TSM conductive framework, which would provide high carrier mobilities and electrons with unconventional energy dispersions, known to result in noncollinear magnetism (Fig. 1b). This approach, applied to bulk crystalline intermetallics, allowed us to identify the air-stable noncoplanar magnets Dy_3Sn_7 and Tb_3Sn_7.

Dy_3Sn_7 and Tb_3Sn_7, while previously reported in powder form, to date have neither been obtained as single crystals, nor have seen a detailed physical property study. Here, we report both. The materials are ultra-pure metals, with residual resistivity ratios of ≈200 and longitudinal conductivities on the level of 100,000 $\Omega^{-1}\,cm^{-1}$, and high charge carrier mobilities, reaching values above 17,000 $cm^2\,V^{-1}\,s^{-1}$. Critically, they also host a complex array of magnetic phases, with a giant Hall anomaly arising in the noncoplanar magnetic phase of the material. We report one of the highest anomalous Hall conductivities, ≈ 42,000 $\Omega^{-1}\,cm^{-1}$, along with an uncommonly high Hall angle of 0.17 (Fig. 1c).

Although the materials we report order only at cryogenic temperatures, and thus have no direct applications in data storage, our strategy is potentially extendable to d-metal magnets, which feature room-temperature magnetism. Thus, this work represents the first step towards the intelligent design of complex magnets for data storage.

Results

Chemical design of a noncoplanar magnet

Whereas many areas of materials science have enjoyed the benefits of large-scale ab initio screening[12–14], reliable prediction of magnetic structures still remains challenging. Magnetic moments often adopt much larger unit cells than the parent nuclear structures, and that is even more dramatic for noncollinear magnets. The complexity drastically increases the computational power required, prohibiting reliable predictions of magnetic order for even a single material. Chemical knowledge and intuition are then uniquely powerful tools for the design of complex magnets. We will use them to select the layers of our target magnet, by focusing on three key elements: magnetic anisotropy, topological bands, and exchange interactions.

The preferred orientation of a magnetic moment in space, in the absence of exchange, is shaped by the fine splitting of the magnetic states due to their crystallographic environment. This produces magnetocrystalline anisotropy (MCA), which can be reliably understood, for both d and f metals, on the basis of their closest crystallographic environment. We can use this information to identify the dissimilar magnetic sublattices that constitute the first set of layers in our strategy (Fig. 1a): e.g., if one layer has an axial anisotropy along one direction, we would need to ensure the other layer would not. The strength of the MCA, similar to other spin-orbit coupling effects, increases with the atomic number, being strongest in heavier elements such as second or third-row transition metals or lanthanides. This, along with their strongly localized moments, make the lanthanides the simplest target to test our strategy—however, we see no reason why it would not be extendable to transition metals, which can enable room-temperature magnetism.

In materials with strongly localized magnetic moments, Ruderman–Kasuya–Kittel–Yosida (RKKY) exchange[15–17] tends to be prevalent. Notably, RKKY exchange has an oscillatory dependence on distance between magnetic ions, and a close connection to the electronic structure of materials. These two factors tend to produce complex spin structures in RKKY materials, including noncoplanar magnets[6,7,18,19]. Specifically, RKKY interactions in TSMs can engender

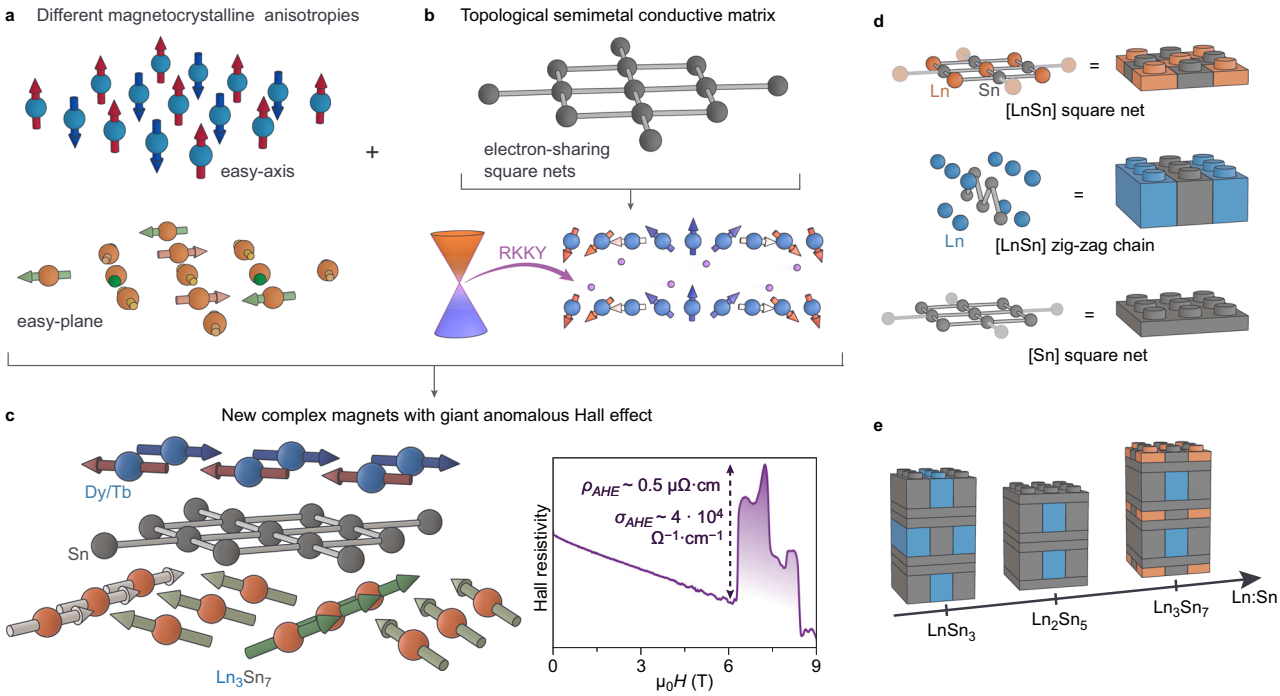

Fig. 1 | Chemical design of a noncoplanar magnet. a, **b** Noncoplanar magnets are promising for data storage applications, but are usually only discovered serendipitously. Here, we design such a magnet by combining three structural elements: **a** Two-layer blocks with magnetic ions in different crystallographic environments, which force different magnetic anisotropies and, thus, directionalities of magnetic order. **b** A topological semimetal (TSM) conductive layer that would allow the two blocks to order through RKKY interactions. **c** The combination of these three elements produced noncoplanar magnets Ln_3Sn_7 with a giant Hall effect anomaly. **d**, **e** To implement this strategy, we investigated the Ln_nSn_{2n+1} family of intermetallics. It possesses all of the required elements. **d** All structures in the family are composed of two [LnSn] lattices, with the lanthanides in very different orientations, and the [Sn] square net, providing possible TSM states. **e** Different stackings of the blocks can be achieved by controlling the Ln:Sn ratio. Ln_3Sn_7 is the simplest member of the family to have all three blocks and was the subject of this study.

https://doi.org/10.1038/s41467-024-54203-3

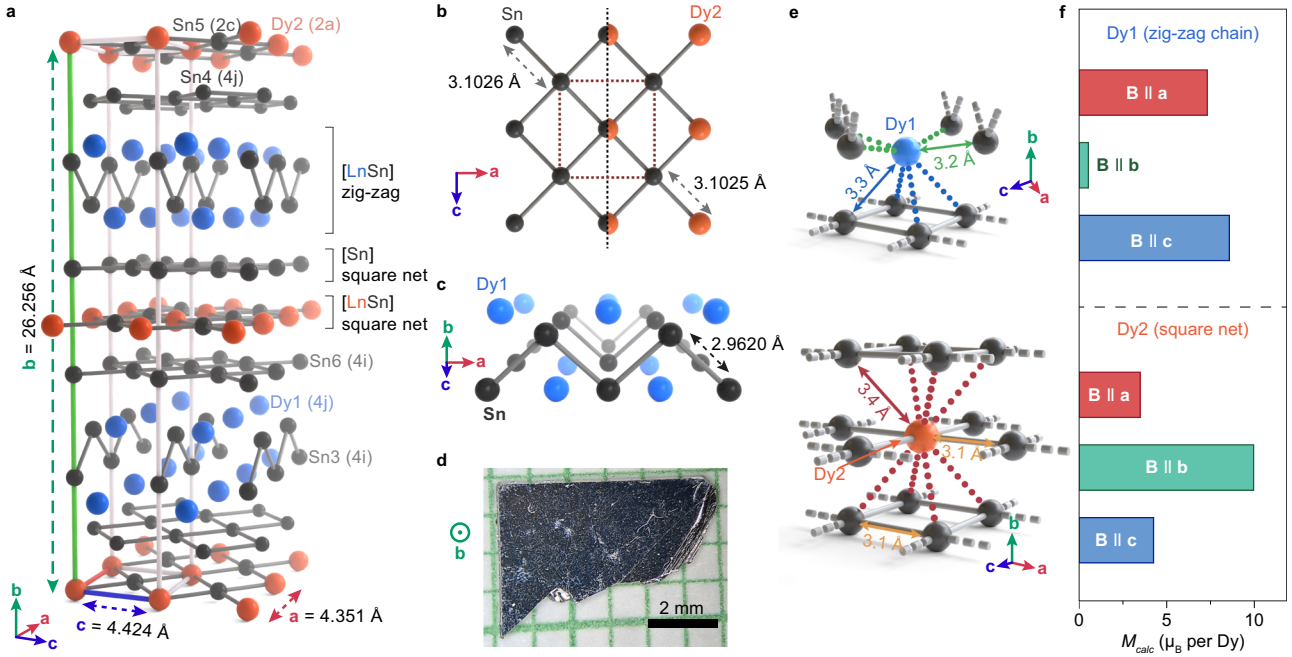

Fig. 2 | Noncoplanar magnets Ln_3Sn_7. a–c The structure (**a**) of Ln_3Sn_7 (here shown for Ln = Dy) can be separated into three units: tin square nets (**b**, left), tin-dysprosium mixed square nets (**b**, right), and dysprosium/tin zig-zag chains (**c**). Bonds are drawn for all contacts shorter than 3.15 Å. Wyckoff symbols are shown for all symmetrically independent atoms. **d** We grew Ln_3Sn_7 as millimeter-scale plate-like single crystals, allowing for detailed magnetotransport studies. **e** Different coordination environments of the two non-equivalent lanthanide sites force their magnetocrystalline anisotropies to be near-orthogonal: whereas the zig-zag chain atoms Dy1 have a very hard **b** axis and easy **ac** plane, the square-net atom Dy2 has a clear soft **b** axis. **f** Bar chart shows expected magnetic moments for each site at 9 T and 1.8 K, calculated using a point-charge model (see Methods for more information). Each bar represents a single data point.

more complex magnetic orders, including noncoplanar textures[19–23]. Topological electronic states are heavily studied for their very high charge carrier mobilities and unique electromagnetic responses, however their interactions with magnetism are not fully understood. Yet, several recent reports provide strong theoretical[20–23] and experimental[19] links between the topologically protected Dirac or Weyl fermions and noncollinear magnetism in TSM RKKY magnets.

Previously, we and others have demonstrated that chemical knowledge can be used to predict TSM states—by targeting intermetallics featuring certain structural motifs with hypervalent bonding, including linear chains, square nets or kagome lattices, of post-transition metals[24–26]. Such motifs may be the optimal pairing to the dissimilar magnetic sublattices, and could enable both complex RKKY magnetism and high-mobility charge transport (Fig. 1b). Although we believe that any of these hypervalent motifs can, in principle, produce a viable material with our strategy, in this work we focused on square nets of tin, as the square net motif has so far provided one of the most chemically diverse and robust sets of TSMs[24]. Furthermore, a preference for square net systems for noncoplanar textures, especially spin vortices[27], has been linked to the high tetragonal symmetry of this lattice motif. Altogether, the key elements of our strategy can be summarized as follows: (1) at least two separate sublattices of magnetic ions in different crystallographic environments; (2) a post-transition metal sublattice featuring the hypervalent square-net motif.

Binary lanthanide tin intermetallics offer a broad space to test our approach. Specifically, the Ln_nSn_{2n+1} family[28–32] is all composed of three types of structural layers: the [LnSn] mixed square net, the [LnSn] zig-zag chain array, and the [Sn] square net (Fig. 1d). These represent a complete set of elements required by our strategy: the two [LnSn] blocks have the lanthanides in very different crystallographic environments, leading to different single-ion anisotropies; the tin square net can provide a TSM state. By simply varying the Ln:Sn ratio, we can precisely control which of these blocks are included in the compound, and how they are stacked (Fig. 1e). In this study, we report Ln_3Sn_7 (Ln = Dy, Tb), which is the simplest structure of the family that contains the two different [LnSn] blocks along with the [Sn] square net.

Structure of Ln_3Sn_7

We synthesized millimeter-scale crystals of Ln_3Sn_7 (Fig. 2d) using self-flux growth, and, using single-crystal X-ray diffraction, confirmed the previously reported crystal structure[28,30]. Figure 2a shows the structure of Dy_3Sn_7, in the centrosymmetric space group Cmmm. If we consider only the closest bonding contacts, the structure readily separates into three stacked layers: the tin square net (Fig. 2b, left), the tin-lanthanide square net (Fig. 2b, right), and the zig-zag chains of tin and the lanthanide (Fig. 2c). These blocks provide us with the three elements we are looking for: the two different magnetic sublattices, and a conductive layer to connect them and allow RKKY exchange.

The lanthanide blocks are expected to favor magnetic order with different magnetic moment directions due to differences in MCA. The crystal lattice forces the square-net lanthanide atoms Ln2 to be the same size laterally as the tin atoms they are bonded to, significantly constricting them compared to the zig-zag chain sublattice Ln1. To obtain a qualitative estimate of this difference, we employed the pyPointCharge package to perform point-charge calculations (see Methods for more detail). We found that Ln2 is expected to have an easy axis along the crystallographic **b** axis (Fig. 2e for Dy_3Sn_7, Supplementary Fig. 6A for Tb_3Sn_7), meaning that the magnetic moments on Ln2 favor orienting along **b**. On the other hand, the zig-zag chain Ln1 atoms are easy-plane within the **ac** plane (and thus have a very hard axis parallel to **b**). This difference in orientations could help us reach noncoplanar states that require finite magnetic moments in all three directions.

The tin square nets in the material have a suitable geometry for the appearance of a TSM state. We previously reported the use of a geometrical tolerance factor that aids in the prediction of TSM states in square net compounds[24]: $t = d_{sq}/d_{nn}$, where d_{sq} is the distance between the square-net atoms, and d_{nn} is the distance between a square-net atom and its closest non-square-net neighbor. For both

https://doi.org/10.1038/s41467-024-54203-3

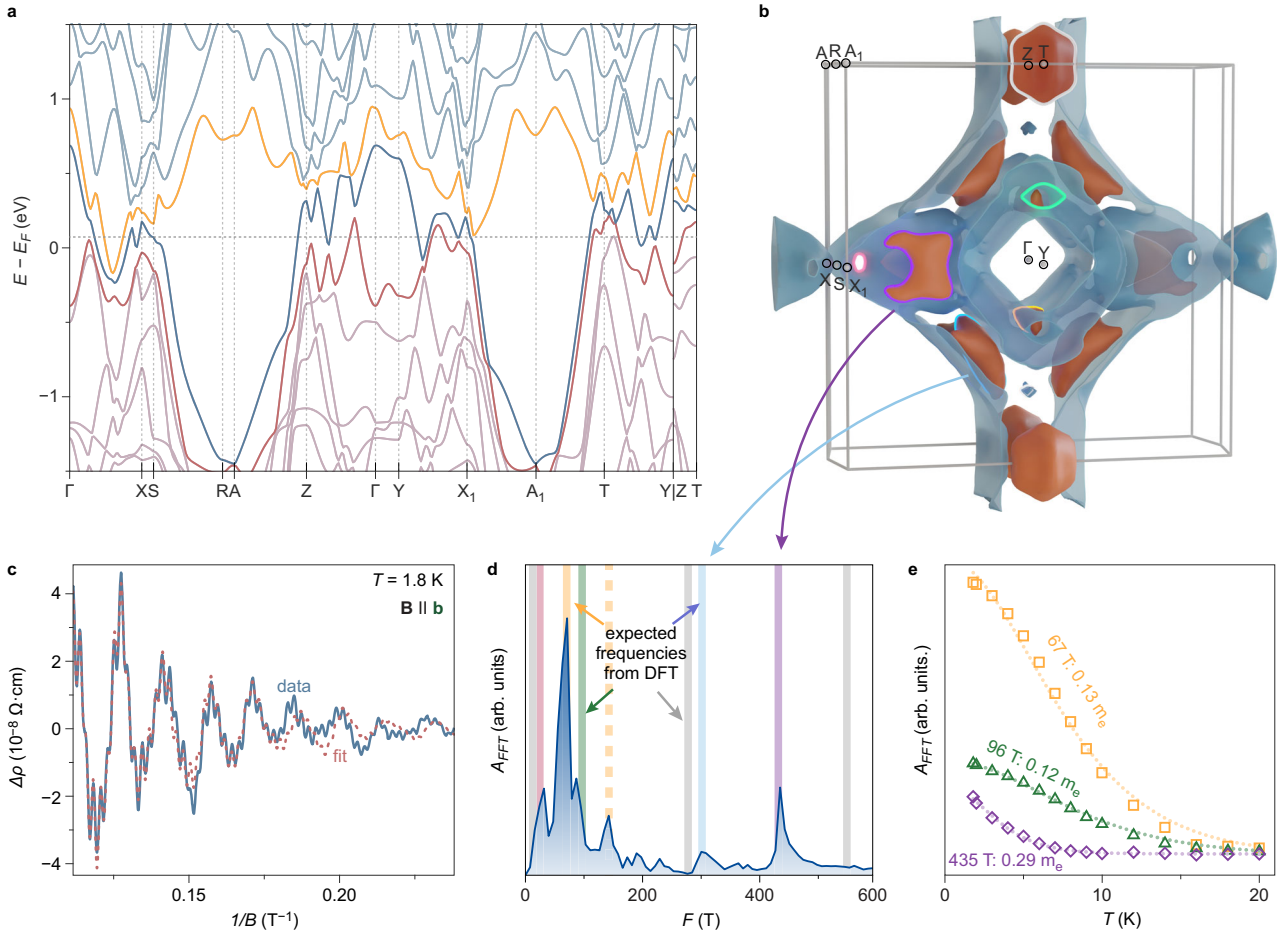

Fig. 3 | Expected electronic properties of Dy_3Sn_7. a The computed electronic band structure of the material is complex due to the low symmetry (space group Cmmm) and relatively large volume (≈500 Å^3) of the structure. Both Dy_3Sn_7 and Tb_3Sn_7 are calculated to be enforced semimetals, with topologically protected states even if an electron was added or removed from the system (see Supplementary Note 3 for more detail). **b** Three bands cross the Fermi level and produce a complex Fermi surface with multiple pockets (colors on the plot match the corresponding bands from **a**). The sharp dispersion at the gapped-out crossing results in very small pockets, which could lead to long-wavelength RKKY magnetic structures. **c** Experimentally, we observed pronounced Shubnikov–de Haas oscillations in the sample, which can be fitted to get a close match to the computed band structure (more information provided in Supplementary Note 1). **d** The fast Fourier transform (FFT) frequency spectrum of the oscillations shows most of the orbits predicted by DFT (colored bars represent expected frequencies of the orbits highlighted in neon colors on **b**; dashed line indicates the second harmonic of the 67 T oscillation). **e** The temperature decay of the main observed oscillations provides low effective masses as expected of a TSM. Markers show data, dashed lines indicate fit to Lifshitz–Kosevich temperature decay.

Ln_3Sn_7 compounds, $t = 0.95$, which means that the square nets are well isolated from the surrounding structure, similarly to previously reported confirmed square-net TSMs such as ZrSiS[33,34].

Computed electronic band structures of Ln_3Sn_7 (Fig. 3a for Dy_3Sn_7, Supplementary Fig. 6B for Tb_3Sn_7) show that the materials, in their nonmagnetic states, are enforced semimetals with Fermi degeneracy (ESFD). Due to the presence of both inversion and time-reversal symmetry, all bands are spin degenerate. In the absence of f-electrons, the electron count for both systems is odd; thus, the last occupied band and the first unoccupied are necessarily degenerate. We can also analyze the topology of the system when an electron is added or removed, that is, if we shift the Fermi level above the doubly degenerate band or below. The structure remains topologically nontrivial in both cases, meaning that it is not simply due to the odd filling of the electronic bands. The electronic structures of both materials feature several band crossings near the Fermi level, characteristic of TSMs, and resulting in very small pockets in the Fermi surface (Fig. 3b shows Fermi surface with E_F adjusted by +73 meV, to match experimental quantum oscillations). One of the hallmarks of a TSM is the high carrier mobilities and low effective masses, which stem from the relativistic Dirac or Weyl dispersion. Often, this leads to observations of strong quantum oscillations, which are characteristic of low-defect high-mobility metals. Indeed, in single-crystal electrical transport devices of both Ln_3Sn_7 materials (as described in further detail below), we observe clear Shubnikov–de Haas oscillations (Fig. 3c–e shows data for Dy_3Sn_7 with magnetic field oriented along the **b** axis; further information is provided in Supplementary Note 1). The observed oscillation frequencies can be matched well to the calculated Fermi surface; fitting of the temperature decay of the main oscillation amplitudes provides very low effective masses of 0.13 m_e (67 T), 0.13 m_e (96 T) and 0.29 m_e (435 T). From full fits of the field-dependent oscillations (Fig. 3c), we extracted high quantum mobilities on the level of 1000–2000 cm^2 V^{-1} s^{-1}. High carrier mobilities were also obtained from Drude model fits of the low-field Hall conductivity, giving values above 17,000 cm^2 V^{-1} s^{-1} (note that quantum mobilities are generally considerably lower than Hall mobilities). Although the band structures of Ln_3Sn_7 may appear complex, evidently, Ln_3Sn_7 host the low carrier masses and high carrier mobilities, signatures of TSMs—and thus further validate our approach.

Magnetic properties of Ln_3Sn_7

Ln_3Sn_7 hosts rich magnetism at low temperatures. When cooled below 20–30 K, the materials undergo a series of magnetic phase transitions, which we observed in the magnetic susceptibility, electrical resistivity, and specific heat, on single crystals of both materials. Figure 4 shows

https://doi.org/10.1038/s41467-024-54203-3

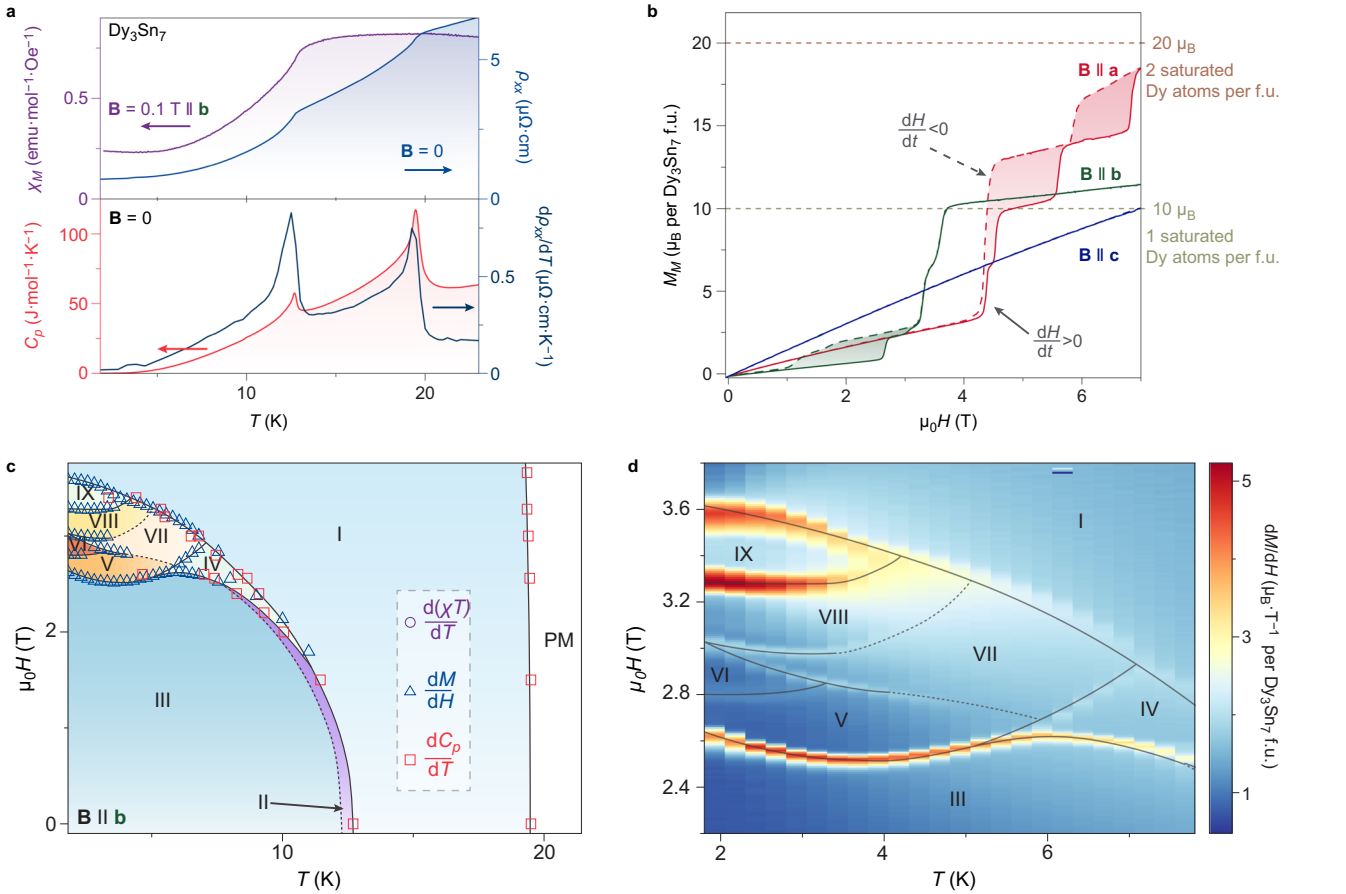

Fig. 4 | Magnetism in Dy_3Sn_7. a Dy_3Sn_7 undergoes three successive magnetic phase transitions at low applied magnetic fields: two antiferromagnetic transitions at 19 K and 13 K, very pronounced in magnetic susceptibility and resistivity (top) as well as in specific heat capacity (bottom), and a weak transition at 12.5 K which is only seen as a shoulder in specific heat and a slight change in the slope of the magnetic susceptibility. **b** At low temperatures, Dy_3Sn_7 hosts many field-induced magnetic states, producing sharp step-and-plateau magnetization curves, which are strongly anisotropic with respect to the orientation of the applied field. **c**, **d** We mapped out the magnetic phase diagram (**c**) of Dy_3Sn_7, with the magnetic field applied along the **b** axis, using a combination of magnetic susceptibility–temperature (purple circles), magnetic moment–applied field (blue triangles, also seen in **d**) and specific heat measurements (red squares). The material hosts at least nine different magnetic phases, a large number of which is crowded into a pocket at T < 8 K and 2 T < **B** < 4 T.

the magnetic properties of Dy_3Sn_7, obtained on oriented single crystals using SQUID or vibrating sample magnetometry (see Methods for more detail). At low applied magnetic fields, two clear transitions manifest themselves as drops in electrical resistivity and magnetic susceptibility (Fig. 4a), suggesting that the ordered phases are antiferromagnetic in character. Strong coupling between the electronic and magnetic structures in RKKY materials tends to produce a considerable drop in longitudinal resistivity at temperatures matching the magnetic transitions. Indeed, the temperature derivative of the resistivity follows closely the trend of the specific heat capacity, as is often seen in RKKY metals. Also prominent in the resistivity is the strength of the drop at low temperatures: we observe residual resistivity ratios $RRR = \frac{R_{300K}}{R_{4K}} = 50–200$ across the different crystals, which puts the materials solidly in the ultra-pure domain.

When a strong external magnetic field is applied to the crystals, Dy_3Sn_7 undergoes a cascade of step-like magnetic transitions (Fig. 4b). These transitions have a strong dependence on the orientation of the magnetic field: the **c** axis is the hardest with no field-induced transitions below 7 T; **a** and **b** axes, however, have a similar step-and-plateau field dependence, with some transitions showing strong hysteresis. This results in a very complex magnetic phase diagram; to investigate it, we mapped out all states occurring in Dy_3Sn_7 below 7 T, with field along the **b** axis, using a combination of magnetization, susceptibility, and specific heat sweeps, which we show in Fig. 4c, d. Clear first-order phase transitions separate three regions of the field-temperature space: the high-temperature and high-field phase I, the low-temperature low-field phase III, and the complex multi-phase space in-between I and III—whereas the transitions within the latter are considerably less pronounced.

Similar magnetization plateaus are sometimes observed in Ising systems, where each step corresponds to a flip of some of the antiferromagnetically ordered spins to align with the field orientation—which in extreme cases may produce so-called devil's staircases[35]. These are well-known in lanthanide magnets, with some examples including $TiNi_2Si_2$[36,37] and CeSb[38,39]. Unique about Dy_3Sn_7, however, is that the same step-like dependence is observed along two symmetrically and structurally non-equivalent directions (**a** and **b**). We believe this is likely due to the field preferentially affecting one or the other Ln sublattice depending on the magnetic field. This is supported by the saturation magnetization achieved along the different directions: for the formula unit Dy_3Sn_7, one Dy atom belongs to the square-net sublattice, and the other two to the zig-zag chains. Indeed, when the field is aligned along the **b** axis, the magnetization reaches a saturation moment of $\approx 11\mu_B$ per Dy_3Sn_7 formula unit at 7 T (i.e., per three Dy atoms), which can correspond to one Dy atom fully magnetized (10 μ_B) and two Dy atoms carrying a net moment of near-zero (e.g., fully antiparallel)—and would also align with our computational prediction of the square-net Dy atoms having an easy **b** axis. When the field is aligned along the **a** axis, however, we see a saturation moment of 18 μ_B, which is close to 20 μ_B that would be expected from the two zig-zag Dy atoms being fully magnetized and the square-net Dy sublattice either

https://doi.org/10.1038/s41467-024-54203-3

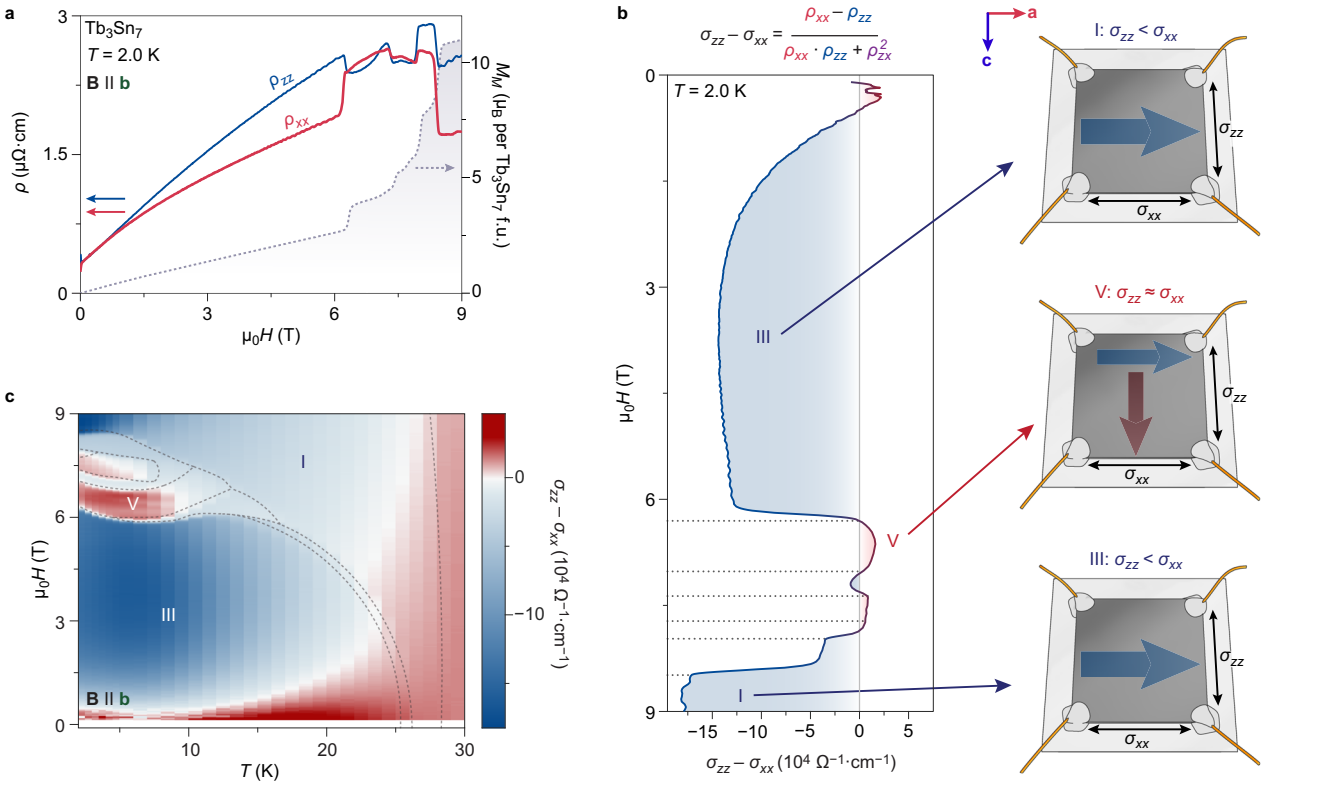

Fig. 5 | Electrical transport in Tb_3Sn_7. **a** Magnetism in RKKY materials is deeply entangled with their electronic properties: electrical resistivity of Tb_3Sn_7 shows sharp transitions matching those observed with magnetometry (right axis). The magnetoresistance also shows a clear anisotropy within the crystallographic **ac** (square-net) plane, dependent on the direction of the applied current. **b** This anisotropy can be quantified with the differential conductivity σ_{zz}–σ_{xx}. This value is negative in phases I and III, meaning that transport along the **c** axis is suppressed in those phases, whereas in phases V–VIII, the ac plane becomes isotropic. **c** Indeed, the higher symmetry appears to be strongly localized to the phases within the complex magnetic pocket of the magnetic phase diagram, with a maximum in phase V. It is likely that these changes are magnetic in origin, and can mean that phase V has magnetic order with finite components along both **a** and **c** axes, and thus more likely to be noncoplanar. Red and blue arrows in the illustrations represent the predominant components of the conductivity tensor along the two in-plane directions.

being fully disordered or being fully antiferromagnetically ordered and carrying zero net moments.

Despite its different electron count and, thus spin state, the terbium analog Tb_3Sn_7 shows similar magnetism to Dy_3Sn_7. Both the low-field (Supplementary Fig. 7A) and high-field (Supplementary Fig. 7B) properties of Tb_3Sn_7 match well to those of Dy_3Sn_7, but are scaled to higher fields and temperatures, as would generally be expected for RKKY magnets with such spin states. The similarity is even more apparent when the magnetic phase diagrams are compared side-by-side (Supplementary Fig. 8). To gain a better understanding of the magnetism within both materials, and see if signatures of noncoplanar magnetism are visible, we continued with a single-crystal electrical transport study.

Electrical transport of Ln_3Sn_7

In RKKY materials, magnetic and electronic structures are intricately connected, causing a particularly strong dependence of their electronic transport on magnetism. To leverage this connection, we fabricated single-crystal electrical transport devices and further probed the magnetic structures in Ln_3Sn_7. On oriented crystals, we employed the Montgomery geometry[40], which is a derivative of the van der Pauw method, to distinguish the two diagonal components of the **ac** plane resistivity tensor ρ_{xx} and ρ_{zz}. The data shown represent the intrinsic resistivities or conductivities of the materials, corrected for sample geometry; similar results were obtained for multiple batches and crystals, and also in the linear 6-wire geometry (Supplementary Fig. 5). Figure 5 shows the response of the electrical resistivity of Tb_3Sn_7 to an external magnetic field applied along the **b** axis. Dy_3Sn_7 shows qualitatively similar behavior, as we present in Supplementary Fig. 9.

Longitudinal magnetoresistance of Tb_3Sn_7 shows sharp transitions at fields matching the steps in magnetization (Fig. 5a). The general shape of the features is consistent between Tb_3Sn_7 and Dy_3Sn_7 (Supplementary Fig. 9A), mirroring the results of the other measurements. These sharp transitions were consistently observed across multiple crystals and multiple batches. Although in zero-field conditions, resistivities along the **a** and **c** axes are similar, application of a magnetic field along the **b** axis resulted in a clear and consistent anisotropy within the **ac** plane: ρ_{xx}, measured with electrical current oriented along the **a** axis, is ~20% lower than ρ_{zz} (**I**||**c**) at high fields (>4 T for Dy_3Sn_7 and > 8.5 T for Tb_3Sn_7), in magnetic phase I.

We explored this anisotropy further by considering the differential conductivity σ_{zz}–σ_{xx} (Fig. 5b), needing to invert the resistivity tensor as conductivity is directly proportional to the relevant quantities affected by magnetic order, such as scattering time, carrier mobility or carrier concentration. This metric would be close to zero for phases with symmetric in-plane transport, and non-zero for asymmetric, such as phase I as discussed above. Figure 5c shows the differential conductivity mapped onto the temperature-field space, with overlaid dashed lines showing the magnetic phase boundaries determined using other methods as in Fig. 4c and Supplementary Fig. 8. For both materials, phases within the complex region (V–VIII for Tb_3Sn_7) are considerably more symmetric in the **ac** plane than the surrounding phases I or III. This anisotropy likely stems from magnetic order, and we can use this anisotropy to get a preliminary picture of the magnetic order within Tb_3Sn_7. Recent research[41,42] suggests that

https://doi.org/10.1038/s41467-024-54203-3

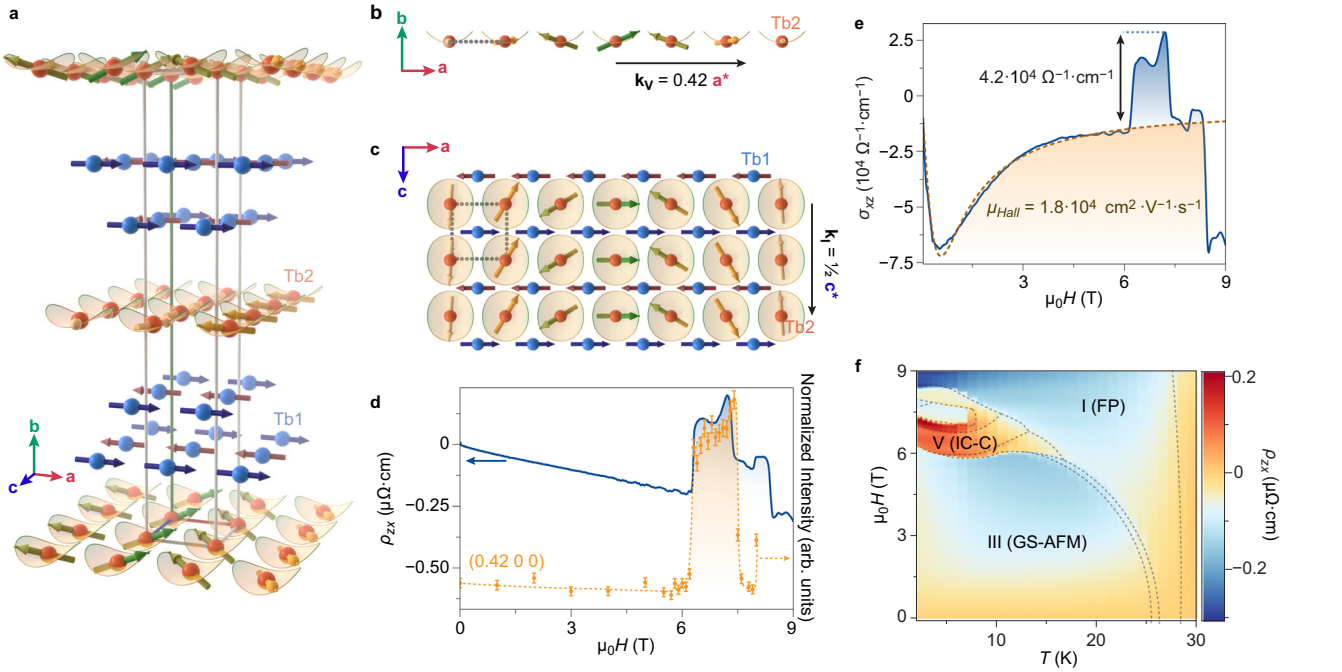

Fig. 6 | Magnetic structure of the incommensurate conical phase (V) of Tb_3Sn_7. **a** Phase V (IC-C) adopts an incommensurate noncoplanar magnetic structure with two separately ordered Tb sublattices. The zig-zag chain Tb atoms order antiferromagnetically with the propagation vector $\mathbf{k_I} = \frac{1}{2}\mathbf{c}^*$. Within each chain, the Tb moments coalign along the **a** axis, and this direction flips along **c**. **b** The square-net Tb moments form a noncoplanar conical state with $\mathbf{k_V} = 0.42(2)\mathbf{a}^*$. **c** The projection of the structure along the **b** axis shows the complex arrangement of the moments between the two sublattices. Note that **a**–**c** omit the tin atoms for clarity. **d** The IC-C phase has a clear and strong signature in the Hall effect of the material. The Hall resistivity in this phase sharply changes its sign; the strength of this anomaly follows closely the intensity of the neutron scattering reflections corresponding to $\mathbf{k_V}$. Error bars represent the square root of observed counts, propagated during data normalization, correction, and integration using conventional error propagation. **e** By fitting the low-field Hall conductivity of the device with the Drude model, we can extract the anomalous Hall conductivity (AHC) corresponding to the IC-C anomaly. This value reaches ≈42,000 Ω^{-1} cm^{-1}, which is one of the highest observed for bulk systems, and, to the best of our knowledge the single highest in a non-collinear or noncoplanar magnetic phase; also prominent is the Hall angle, with $\tan\theta_H \approx 0.11$ for the device shown, uncommonly high for materials showing comparable AHCs. **f** Mapping the Hall effect to the magnetic phase diagram of the material shows that the Hall anomaly is indeed a sharply contained signature of the magnetic order, similar to topological Hall effect in skyrmion lattices.

magnetoresistance in antiferromagnets can be phenomenologically described as proportional to $\sum_i(\mathbf{j}\cdot\mathbf{m_i})^2$, where **j** is the direction of the electrical current, and $\mathbf{m_i}$ are the magnetic moments of the lattice. With this model, we can propose that magnetoresistance anisotropy may arise in Tb_3Sn_7 if one of the magnetic sublattices is oriented along the **b** axis (parallel to the magnetic field), and the other sublattice is oriented along either **a** or **c**. Magnetoresistance will then be seen when the current is parallel to the orientation of the moments in the latter sublattice, but not when it is orthogonal, as is observed in phases I and III. If a spin-flop transition then turns the first sublattice into the **ac** plane, we can then expect the anisotropy to be partially canceled out—as is the case in phase V. Accordingly, phase V presents a strong candidate for non-collinear magnetism. We explored this possibility further by performing in-field single-crystal neutron scattering (see Supplementary Note 2 and Supplementary Fig. 10 for more detail on data collection and refinement).

Magnetic structure of the incommensurate conical phase (V) of Tb_3Sn_7

Figure 6a shows the magnetic structure of the incommensurate conical (IC-C) phase V, solved and refined in the magnetic superspace group A2'aa'(00γ)0s0, obtained through refinement of single-crystal unpolarized neutron scattering data (see Supplementary Information for more detail). The structure requires three propagation vectors, $\mathbf{k_I} = \frac{1}{2}\mathbf{c}^*$, $\mathbf{k_V} = 0.42(2)\mathbf{a}^*$ and $\mathbf{k_0} = 0$. Weak second and third harmonics of $\mathbf{k_V}$ were also observed. The commensurate $\mathbf{k_I}$ component describes the order within the zig-zag sublattice, which is a simple collinear antiferromagnet: along each zig-zag chain, spins are coaligned, but these orientations alternate along the **c** axis. The $\mathbf{k_V}$ and $\mathbf{k_0}$ components correspond to the much more complex incommensurate order in the mixed square-net plane. The moments in this sublattice adopt a constant moment state (Fig. 6b, c), where the **a** and **c** axis components of each neighboring moment are almost antiparallel, and carry no net magnetization, whereas the moment along the **b** axis (described by the $\mathbf{k_0}$ component) is mostly positive, resulting in a net moment of 1.24(8)μ_B. This is comparable to the value obtained from magnetometry, which is ≈1.1μ_B if we subtract a linear antiferromagnetic component. We note that this state is not an ideal conical state, as the ordering defined by the second and third harmonics leads to a distortion that produces the displayed petal-like surface. The two sublattices combined produce an even more complex noncoplanar texture (Fig. 6c), as intended with our strategy.

The neutron structures also confirmed our suspicions regarding the origin of the transport anisotropy. Across the magnetic phase diagram, the Tb1 (zig-zag) sublattice retains the same $\mathbf{k_I}$ commensurate antiferromagnetic order. The changes observed with magnetometry, transport, and other methods originate instead in rearrangements of the moments belonging to the square-net Tb2 sublattice. In the ground-state phase III (GS-AFM, Supplementary Fig. 11A, B), they order antiferromagnetically; all Tb2 moments there orient along the **b** axis, with directions alternating along **a** and **b**. In the field-polarized phase I (FP, Supplementary Fig. 11C, D), the Tb2 moments again orient with the direction of the field, along the **b** axis. Only in the IC-C phase do the Tb2 moments have finite components within the **ac** plane, producing the isotropic electronic transport.

The IC-C phase also displays a strong and sharp anomalous Hall effect (AHE) (Fig. 6d). We extracted the magnitude of this anomaly by fitting the low-field Hall conductivity to the Drude model, leaving an anomalous Hall conductivity (AHC) close to 42,000 Ω^{-1} cm^{-1} at 7.2 T

(Fig. 6e). This AHC is one of the largest reported to date for bulk crystals, and over an order of magnitude stronger than what has been reported for Fe thin films[43] and $Co_3Sn_2S_2$[44], which are often used to benchmark AHE. Similar results have been associated only with skew scattering in very good metals in their non-magnetic or field-polarized states—and the longitudinal conductivity of Tb_3Sn_7 at 7.2 T is ~378,000 Ω^{-1} cm^{-1}, which is usually considered sufficient for skew scattering to dominate the AHE[45–47]. Interestingly, in such materials, the Hall angle is usually very low, with anomalous Hall ratios ($AHR = \sigma_{AHE}/\sigma_{xx}$) of less than 0.01[48]. For Tb_3Sn_7, however, the AHR is much higher, reaching values as high as 0.17. This combination of high AHR and AHC is very rare[48–50], and, to the best of our knowledge, has never been observed in a system with complex magnetic order. Notably, this can be favorable for memory applications as high longitudinal conductivities can reduce resistive energy losses while maintaining a strong Hall response.

The strength of the Hall effect anomaly follows precisely the intensity of the magnetic reflections corresponding to $\mathbf{k_V}$ (Fig. 6d). If we map the Hall resistivity to the magnetic phase diagram (Fig. 6f), it is further apparent that the Hall anomaly co-arises with the changes in the square-net magnetic order. It is, however, challenging to pinpoint its specific origin. Let us consider the possible explanations. First, we will consider intrinsic AHE: this appears in materials with significant momentum-space Berry curvature, and thus is most often observed in topological electronic phases such as TSMs. Indeed, here the average symmetry of the IC-C phase (A2'aa') allows for a finite AHC component in σ_{xz}, whereas the GS-AFM phase, which adopts magnetic space group $C_c$mcm, has zero Berry curvature (see Supplementary Note 3), and therefore does not display AHE. We should note that intrinsic AHE is generally reported to be on the level of e^2/ha, where e is the elementary charge, h is Planck's constant, and a is the typical lattice cell parameter, which in our case would be ≈1000 Ω^{-1} cm^{-1}; most reports of intrinsic anomalous Hall do not considerably surpass this value[43,44,51]. Thus, the Hall anomaly we observe likely originates in a different effect.

Another frequently invoked explanation is THE. When an electron passes through a real-space texture with non-zero scalar spin chirality (SSC) ($SSC = \boldsymbol{S_1} \cdot \boldsymbol{S_2} \times \boldsymbol{S_3}$, where $\boldsymbol{S_i}$ are different spins), it likewise acquires a Berry phase as in the intrinsic anomalous Hall mechanism, and similarly produces AHE[3,5–7,52,53]. Although the magnetic structure of phase V is noncoplanar and locally some sets of moments in the structure do have finite SSC, the net value over the whole structure is zero, making the THE likewise vanish (Supplementary Note 5; Supplementary Fig. 12A–C). However, recent reports point to another possible origin of the AHE: in SSC-induced skew scattering.

Recently, giant AHE with a Hall ratio of 0.1–0.2 was reported in thin films of MnGe[48]. The effect there was attributed to spin chirality-enhanced skew scattering, arising from SSC-carrying excitations in an otherwise zero-SSC magnetic phase[54]. A similar effect could provide the origin of the unconventional AHE in Ln_3Sn_7. We speculate that magnetic domain boundaries can be the SSC carriers in the material: a simple reversal of the propagation vector can provide a finite SSC across such a boundary (Supplementary Note 5; Supplementary Fig. 12D, E). Such scattering may be possible due to the very long carrier mean paths in Ln_3Sn_7: using the effective masses and mobilities from electrical transport and Fermi velocities from density function theory (DFT) calculations, we obtain values between 30 and 300 nm, which may be sufficiently large to enable scattering off of boundaries. Additional evidence towards a skew-scattering origin of the Hall effect anomaly comes from the scaling of the AHC with the longitudinal conductivity (Supplementary Fig. 13). We have performed Hall effect measurements on 11 crystals of Tb_3Sn_7 and 5 crystals of Dy_3Sn_7, and observed a roughly linear dependence of the AHC on σ_{xx} in both cases, giving a high anomalous Hall angle of 0.17 for Tb_3Sn_7. A dependence of the AHC on the longitudinal conductivity would be expected only in the case of skew-scattering originated AHE, and not for intrinsic AHE, where the AHC is expected to be invariant of σ_{xx}[47]. Together with the AHC being unlikely high for intrinsic AHE, we believe SSC-enhanced skew scattering to be a probable origin for this anomaly.

Regardless of the specific origin however, we would like to highlight that the strong AHC was enabled by our design strategy. Indeed, only through the inclusion of the square-net sublattice could we expect the long mean free paths that we invoke in SSC-induced skew scattering; and the same square-net sublattice provides us with Weyl nodes for reciprocal-space Berry curvature. Through the combination of our two material design elements, we obtained a noncoplanar magnetic phase with a strong a clear transport signature in AHE.

Discussion

Search for new noncoplanar magnets is a challenging direction in modern solid-state chemistry and physics—but is also one with a big payoff, due to the possible applications in computer memory and elsewhere. For those applications, many reports focused on complex magnets with Hall effect signatures. Here, we report noncoplanar magnets with some of the strongest Hall anomalies seen to date that can serve as specific signatures of the magnetic order. Our materials could, on their own, serve as a platform for further study: one avenue would perhaps be seeing how the mixing of dysprosium and terbium, and thus the spin state, can be used to control the magnetism. Also interesting is comparison to tellurides and antimonides with related structures: the tellurides have been reported by us and others to produce complex magnetism and topological states[55–58], however no clear Hall effect anomaly has been observed in any of them. One possibility may lie in the mixed square-net layer that does not appear in the tellurides or antimonides. Only a detailed study of the different Ln_nSn_{2n+1} compounds would allow a more complete answer.

But beyond that, we report an approach towards the intentional search or design of such magnets. The considerations we applied can be used by chemists to screen promising systems manually; they may see applications beyond bulk single crystals: the layered structure of our designed material yields just as well—or perhaps, even better—to fabrication of van der Waals or epitaxial heterostructures. It can also be effectively translated to large-scale data processing operations. Indeed, it is easy to envision a structure-search algorithm that would look for materials with several component sublattices of lanthanides or other magnetic ions and produce a rough estimate of their MCAs through point-charge calculations. Then, through either considering their already known topological classification, or by searching for structural motifs that are especially likely to host topological state—e.g., square nets, linear chains, or kagome frameworks—we can select the optimal candidates.

A vast number of materials have been cataloged in structural databases, yet relatively few have seen a detailed physical property study. Indeed, despite the simple binary chemistry and initial reports dating some thirty years back, this is the first study of magnetism in Tb_3Sn_7 and Dy_3Sn_7. With recent advances that added millions more stable materials to consider[59], it is clear that chemical strategies like ours are crucial for the discovery of exciting new physics within them.

Methods

Synthesis

Millimeter-scale single crystals of Dy_3Sn_7 and Tb_3Sn_7 were synthesized using tin self-flux growth. The phase diagram of the Dy–Sn and Tb–Sn systems is complex, and necessitated a large excess of tin (50 to 100 times) to obtain Ln_3Sn_7. In a typical reaction, 1–1.5 mmol dysprosium or terbium pieces (99.8+%, Thermo Fisher Scientific) are combined with 198.5–199 mmol tin shot (99.999+%, Strem Chemicals), sealed under vacuum within a borosilicate glass ampule (16 mm inner diameter) fitted with a wad of glass wool. The reaction vessel is then transferred, upright, into a box furnace, where it is quickly heated to 850 °C, kept at that temperature for 48 hours, and cooled to 450–500 °C at a rate of 1–2 °C per hour. The vessel is then inverted and

centrifuged, with a peak relative centrifugal force of ≈200 × *g*, to separate the crystals from the flux (consisting mostly of remaining tin), which passes through the wad of glass wool. This procedure usually yields 100–800 mg of Ln_3Sn_7 as plate-like shiny crystals, several millimeters in lateral dimension and a few hundred micron in thickness. In some cases, significant amounts of residual tin flux remained attached to the crystals, which were removed either mechanically with 100–2000 grit sandpaper, or chemically by etching for ~30 minutes with a 5% hydrogen peroxide solution in 5 M aqueous sodium hydroxide. No significant difference was observed in the structural or physical properties of crystals processed with either method. The crystals are relatively air-stable, and maintain their physical properties after a prolonged air exposure of at least several weeks, however, for the purposes of this study we generally kept the crystals in a dry argon-filled glove box.

Structural characterization

To confirm the reported structures of Ln_3Sn_7, we used single-crystal X-ray diffraction with Mo K_α radiation (Bruker-AXS D8 Venture 4-circle diffractometer with an APEX2 CCD detector). As-synthesized crystals proved too large for diffraction analysis, and were cut manually to reduce the lateral dimensions below 100 μm. Diffraction patterns were collected at 100 K under a nitrogen cryojet, and were integrated using SAINT, scaled and corrected for absorption with SADABS, as implemented in the Bruker APEX2 suite. A data solution was found using ShelXT[60], confirming the reported structure in space group Cmmm, and was refined using ShelXL[60], assisted by the graphical interface ShelXle[61]. For physical measurements, crystals were oriented by face-indexing the crystals at 100 K or 300 K on the same diffractometer.

Density functional theory calculations

DFT calculations were performed as implemented in the Vienna ab initio simulation package[62–65]. More information is provided in Supplementary Note 3. Fermi surfaces of the materials were then obtained using the IFermi package[66], adjusting the Fermi level by +73 meV to match the experimentally obtained quantum oscillations.

Point-charge model calculations

To determine the single-ion anisotropy of the lanthanides in the materials, we used the PyCrystalField package[67]. Crystal structures of Ln_3Sn_7 were loaded using the expected charges of −2 for zig-zag chain tin atoms, −1 for square-net tin atoms, and +3 for the lanthanides. Then, expected magnetic moments were calculated using a temperature of 1.8 K, and an applied magnetic field of 9 T aligned along the principal directions.

Magnetometry

To measure magnetic susceptibility and magnetization of Ln_3Sn_7, we used a Quantum Design (QD) 7 T MPMS, or a QD 14 T PPMS. We mounted oriented single crystals of the materials, weighing, usually, 1–20 mg, on quartz paddles or rods with GE 7031 varnish, and measured a sequence of DC temperature and field-dependent sweeps. Observed data were consistent across multiple crystals and batches.

Specific heat capacity

Specific heat capacity of Ln_3Sn_7 was measured on a QD 9 T PPMS DynaCool using the heat capacity option. Crystals, oriented along the **b** axis and weighing 0.5–10 mg, were mounted on the sample stage using Apiezon N grease.

Single-crystal elastic neutron scattering

Single-crystal neutron diffraction measurements were performed on the cold-neutron time of flight diffractometer WISH[68] at the ISIS neutron and muon spallation source (UK). A 3 × 2 × 0.5 mm single crystal of Tb_3Sn_7 was mounted on an aluminum strip and the crystal was aligned with the **b** axis vertical allowing the collection on the WISH detector of the H0L scattering plane plus a 15 degrees coverage above and below the plane. The zero applied magnetic field data were measured in an ^4He cryostat, whereas the field dependence of the magnetic structure has been measured in a cryo-magnet (restricting the out-of-plane coverage) in the 0–8 T field range with the external magnetic field applied along the **b** axis of the parent paramagnetic structure. Long data collection with two orientations in the H0L plane were collected at 1.5 K, and 0 and 7 T, respectively to solve and refine the magnetic structure in phase I, III and V. Data reduction has been performed using the Mantid software[69]. Data were corrected for Lorentz factor, detector efficiency and normalized by the total synchrotron current and incident flux. The integration of the magnetic and nuclear reflection has been performed in **Q** space using an ellipsoidal region of interest with fixed dimension for all reflections. The refinements of the magnetic and nuclear structure were performed with the JANA2020 software[70], whereas symmetry analysis was performed with the help of the ISOTROPY and ISODISTORT software[71,72].

Electrical transport measurements

Electrical resistivity was measured on oriented single crystals of Ln_3Sn_7, using either a six-wire geometry or the Montgomery method[40,73] to separate the two diagonal components of the resistivity tensor. Similar results were obtained for the two methods. All measurements were performed using a QD 9T PPMS DynaCool fitted with the Electrical Transport Option, which enables low-frequency AC measurements. Crystals were cut to optimal shape manually, using a stainless steel razor blade, and attached to a sapphire chip with GE 7031 varnish. Thin gold wires (25 μm or 50 μm diameter, Alfa Aesar) were then manually attached to the crystals using silver conductive paint (SPI Supplies or DuPont 4929N). Contact resistances were below 2 Ω. The sapphire chip was then secured on the sample stage using silica paste, and the wires soldered to the contact pads. Temperature and field scans were then performed under a low pressure of helium, with a drive current of 10–20 mA applied at frequencies between 3 and 25 Hz. Magnetotransport data were symmetrized (for magnetoresistance) or antisymmetrized (for Hall effect) with respect to magnetic field, combining the positive component for $dH/dt > 0$ and the negative component for $dH/dt < 0$.

Both materials are good metals, with resistivities below 1 mΩ cm at helium temperatures. Residual resistivity ratios $RRR = R_{4K}/R_{300K}$ (calculated at 4 K due to unwanted superconducting contributions of residual tin flux) varied crystal-to-crystal, but were generally on the level of 50–200. Besides variance in RRR, transport properties were consistent across multiple crystals and batches.

Data availability

Additionally, raw data file of the neutron diffraction experiment can be found at https://doi.org/10.5286/ISIS.E.RB2310171. Source data are provided with this paper.

References

1. Fert, A., Reyren, N. & Cros, V. Magnetic skyrmions: advances in physics and potential applications. *Nat. Rev. Mater.* **2**, 1–15 (2017).
2. Fert, A., Cros, V. & Sampaio, J. Skyrmions on the track. *Nat. Nanotechnol.* **8**, 152–156 (2013).
3. Tokura, Y. & Kanazawa, N. Magnetic skyrmion materials. *Chem. Rev.* **121**, 2857–2897 (2021).
4. Tey, M. S. N., Chen, X., Soumyanarayanan, A. & Ho, P. Chiral spin textures for next-generation memory and unconventional computing. *ACS Appl. Electron Mater.* **4**, 5088–5097 (2022).
5. Neubauer, A. et al. Topological Hall effect in the **A** phase of MnSi. *Phys. Rev. Lett.* **102**, 186602 (2009).
6. Hirschberger, M. et al. Skyrmion phase and competing magnetic orders on a breathing kagomé lattice. *Nat. Commun.* **10**, 5831 (2019).

7. Kurumaji, T. et al. Skyrmion lattice with a giant topological Hall effect in a frustrated triangular-lattice magnet. *Science* **365**, 914–918 (2019).
8. Ghimire, N. J. et al. Large anomalous Hall effect in the chiral-lattice antiferromagnet $CoNb_3S_6$. *Nat. Commun.* **9**, 3280 (2018).
9. Nakatsuji, S., Kiyohara, N. & Higo, T. Large anomalous Hall effect in a non-collinear antiferromagnet at room temperature. *Nature* **527**, 212–215 (2015).
10. Chen, T. et al. Anomalous transport due to Weyl fermions in the chiral antiferromagnets Mn_3X, X = Sn, Ge. *Nat. Commun.* **12**, 572 (2021).
11. Šmejkal, L., Jungwirth, T. & Sinova, J. Route towards Dirac and Weyl antiferromagnetic spintronics. *Phys. Status solidi (RRL)—Rapid Res. Lett.* **11**, 1700044 (2017).
12. Jain, A. et al. Commentary: the materials project: a materials genome approach to accelerating materials innovation. *APL Mater.* **1**, 011002 (2013).
13. Bradlyn, B. et al. Topological quantum chemistry. *Nature* **547**, 298–305 (2017).
14. Vergniory, M. G. et al. A complete catalogue of high-quality topological materials. *Nature* **566**, 480–485 (2019).
15. Ruderman, M. A. & Kittel, C. Indirect exchange coupling of nuclear magnetic moments by conduction electrons. *Phys. Rev.* **96**, 99–102 (1954).
16. Kasuya, T. A theory of metallic ferro- and antiferromagnetism on Zener's model. *Prog. Theor. Phys.* **16**, 45–57 (1956).
17. Yosida, K. Magnetic properties of Cu-Mn alloys. *Phys. Rev.* **106**, 893–898 (1957).
18. Machida, Y. et al. Unconventional anomalous hall effect enhanced by a noncoplanar spin texture in the frustrated kondo lattice $Pr_2Ir_2O_7$. *Phys. Rev. Lett.* **98**, 057203 (2007).
19. Gaudet, J. et al. Weyl-mediated helical magnetism in NdAlSi. *Nat. Mater.* **20**, 1650–1656 (2021).
20. Armitage, N., Mele, E. & Vishwanath, A. Weyl and dirac semimetals in three-dimensional solids. *Rev. Mod. Phys.* **90**, 015001 (2018).
21. Araki, Y. & Nomura, K. Spin textures and spin-wave excitations in doped Dirac-Weyl semimetals. *Phys. Rev. B* **93**, 094438 (2016).
22. Chang, H.-R., Zhou, J., Wang, S.-X., Shan, W.-Y. & Xiao, D. RKKY interaction of magnetic impurities in Dirac and Weyl semimetals. *Phys. Rev. B* **92**, 241103 (2015).
23. Hosseini, M. V. & Askari, M. Ruderman-Kittel-Kasuya-Yosida interaction in Weyl semimetals. *Phys. Rev. B* **92**, 224435 (2015).
24. Klemenz, S. et al. The role of delocalized chemical bonding in square-net-based topological semimetals. *J. Am. Chem. Soc.* **142**, 6350–6359 (2020).
25. Yin, J.-X., Lian, B. & Hasan, M. Z. Topological kagome magnets and superconductors. *Nature* **612**, 647–657 (2022).
26. Khoury, J. F. & Schoop, L. M. Chemical bonds in topological materials. *Trends Chem.* **3**, 700–715 (2021).
27. Hayami, S., Ozawa, R. & Motome, Y. Effective bilinear-biquadratic model for noncoplanar ordering in itinerant magnets. *Phys. Rev. B* **95**, 224424 (2017).
28. Venturini, G. & Mesbah, A. An investigation of the structures of the compounds in the tin-rich part of the Dy-Sn system: crystal structure of Dy_5Sn_{11} and Dy_5Sn_{13}. *J. Alloy Compd.* **458**, 22–29 (2008).
29. Meier, K. et al. High-pressure high-temperature synthesis, magnetic properties and X-ray absorption spectroscopy of phases RE_3Sn_7 and hp-$RESn_{3-x}$ (RE = Tb, Ho, Er). *Z. Anorg. Allg. Chem.* **636**, 1695–1702 (2010).
30. Oshchapovsky, I., Pavlyuk, V. & Chumak, I. Tb_3Sn_7: polymorphism and crystal structure of high-temperature modification. *Acta Crystallogr. Sect. B: Struct. Sci. Cryst. Eng. Mater.* **69**, 527–533 (2013).
31. Palenzona, A. & Manfrinetti, P. The tin-rich side of the rare earth-tin systems (R = Gd, Tb, Dy, Ho, Er, Tm, Lu and Y). *J. Alloy Compd.* **201**, 43–47 (1993).
32. Venturini, G., Lemoine, P., Malaman, B. & Ouladdiaf, B. Magnetic structures of orthorhombic rare earth stannides LSn_2 (L=Tb-Tm). *J. Alloy Compd.* **505**, 404–415 (2010).
33. Neupane, M. et al. Observation of topological nodal fermion semimetal phase in ZrSiS. *Phys. Rev. B* **93**, 201104 (2016).
34. Schoop, L. M. et al. Dirac cone protected by non-symmorphic symmetry and three-dimensional Dirac line node in ZrSiS. *Nat. Commun.* **7**, 11696 (2016).
35. Bak, P. & Bruinsma, R. One-dimensional ising model and the complete devil's staircase. *Phys. Rev. Lett.* **49**, 249–251 (1982).
36. Shigeoka, T. et al. Metamagnetism in $TbNi_2Si_2$ single crystal. *J. Phys. Soc. Jpn.* **61**, 4559–4565 (1992).
37. Blanco, J. A., Gignoux, D., Schmitt, D. & Vettier, C. Field induced magnetic structures in $TbNi_2Si_2$. *J. Magn. Magn. Mater.* **97**, 4–14 (1991).
38. Kuroda, K. et al. Devil's staircase transition of the electronic structures in CeSb. *Nat. Commun.* **11**, 2888 (2020).
39. Rossat-Mignod, J. et al. Phase diagram and magnetic structures of CeSb. *Phys. Rev. B* **16**, 440–461 (1977).
40. Montgomery, H. C. Method for measuring electrical resistivity of anisotropic materials. *J. Appl. Phys.* **42**, 2971–2975 (1971).
41. Wadley, P. et al. Electrical switching of an antiferromagnet. *Science* **351**, 587–590 (2016).
42. Shick, A. B., Khmelevskyi, S., Mryasov, O. N., Wunderlich, J. & Jungwirth, T. Spin-orbit coupling induced anisotropy effects in bimetallic antiferromagnets: a route towards antiferromagnetic spintronics. *Phys. Rev. B* **81**, 212409 (2010).
43. Miyasato, T. et al. Crossover behavior of the anomalous hall effect and anomalous nernst effect in itinerant ferromagnets. *Phys. Rev. Lett.* **99**, 086602 (2007).
44. Liu, E. et al. Giant anomalous Hall effect in a ferromagnetic kagome-lattice semimetal. *Nat. Phys.* **14**, 1125–1131 (2018).
45. Onoda, S., Sugimoto, N. & Nagaosa, N. Intrinsic versus extrinsic anomalous hall effect in ferromagnets. *Phys. Rev. Lett.* **97**, 126602 (2006).
46. Onoda, S., Sugimoto, N. & Nagaosa, N. Quantum transport theory of anomalous electric, thermoelectric, and thermal Hall effects in ferromagnets. *Phys. Rev. B* **77**, 165103 (2008).
47. Nagaosa, N., Sinova, J., Onoda, S., MacDonald, A. H. & Ong, N. P. Anomalous Hall effect. *Rev. Mod. Phys.* **82**, 1539–1592 (2010).
48. Fujishiro, Y. et al. Giant anomalous Hall effect from spin-chirality scattering in a chiral magnet. *Nat. Commun.* **12**, 317 (2021).
49. Moya, J. M. et al. Real-space and reciprocal-space topology in the $\mathbf{Eu(Ga_{1-x}Al_x)_4}$ square net system. *Phys. Rev. B* **108**, 064436 (2023).
50. Yang, S.-Y. et al. Giant, unconventional anomalous Hall effect in the metallic frustrated magnet candidate, KV_3Sb_5. *Sci. Adv.* **6**, eabb6003 (2020).
51. Li, P. et al. Giant room temperature anomalous Hall effect and tunable topology in a ferromagnetic topological semimetal Co_2MnAl. *Nat. Commun.* **11**, 3476 (2020).
52. Kanazawa, N. et al. Large topological hall effect in a short-period helimagnet MnGe. *Phys. Rev. Lett.* **106**, 156603 (2011).
53. Singh, C. et al. Higher order exchange driven noncoplanar magnetic state and large anomalous Hall effects in electron doped kagome magnet Mn3Sn. *npj Quantum Mater.* **9**, 1–9 (2024).
54. Ishizuka, H. & Nagaosa, N. Large anomalous Hall effect and spin Hall effect by spin-cluster scattering in the strong-coupling limit. *Phys. Rev. B* **103**, 235148 (2021).
55. Lei, S. et al. Band engineering of dirac semimetals using charge density waves. *Adv. Mater.* **33**, 2101591 (2021).
56. Lei, S. et al. High mobility in a van der Waals layered antiferromagnetic metal. *Sci. Adv.* **6**, eaay6407 (2020).
57. Kogar, A. et al. Light-induced charge density wave in $LaTe_3$. *Nat. Phys.* **16**, 159–163 (2020).

58. Akatsuka, S. et al. Non-coplanar helimagnetism in the layered vander-Waals metal DyTe3. *Nat. Commun.* **15**, 4291 (2024).
59. Merchant, A. et al. Scaling deep learning for materials discovery. *Nature* **624**, 80–85 (2023).
60. Sheldrick, G. M. A short history of SHELX. *Acta Crystallogr. Sect. A: Found. Crystallogr.* **64**, 112–122 (2008).
61. Hübschle, C. B., Sheldrick, G. M. & Dittrich, B. ShelXle: a Qt graphical user interface for SHELXL. *J. Appl. Crystallogr.* **44**, 1281–1284 (2011).
62. Kresse, G. & Hafner, J. Ab initio molecular dynamics for liquid metals. *Phys. Rev. B* **47**, 558–561 (1993).
63. Kresse, G. & Hafner, J. Ab initio molecular-dynamics simulation of the liquid-metal-amorphous-semiconductor transition in germanium. *Phys. Rev. B* **49**, 14251–14269 (1994).
64. Kresse, G. & Furthmüller, J. Efficiency of ab-initio total energy calculations for metals and semiconductors using a plane-wave basis set. *Comput. Mater. Sci.* **6**, 15–50 (1996).
65. Kresse, G. & Furthmüller, J. Efficient iterative schemes for ab initio total-energy calculations using a plane-wave basis set. *Phys. Rev. B* **54**, 11169–11186 (1996).
66. Ganose, A. M., Searle, A., Jain, A. & Griffin, S. M. IFermi: a python library for Fermi surface generation and analysis. *J. Open Source Softw.* **6**, 3089 (2021).
67. Scheie, A. PyCrystalField: software for calculation, analysis and fitting of crystal electric field Hamiltonians. *J. Appl. Crystallogr.* **54**, 356–362 (2021).
68. Chapon, L. C. et al. Wish: the new powder and single crystal magnetic diffractometer on the second target station. *Neutron N.* **22**, 22–25 (2011).
69. Arnold, O. et al. Mantid-data analysis and visualization package for neutron scattering and μ sr experiments. *Nucl. Instrum. Meth. A* **764**, 156–166 (2014).
70. Petříček, V., Palatinus, L., Plášil, J. & Dušek, M. & Jana2020—a new version of the crystallographic computing system Jana. *Z. Kristallogr. Cryst. Mater.* **238**, 271–282 (2023).
71. Campbell, B. J., Stokes, H. T., Tanner, D. E. & Hatch, D. M. ISODISPLACE: a web-based tool for exploring structural distortions. *J. Appl. Crystallogr.* **39**, 607–614 (2006).
72. Stokes, H. T., Tanner, D. E., Hatch, D. & M Campbell, B. J. ISOTROPY Software Suite. iso.byu.edu.
73. dos Santos, C. A. M. et al. Procedure for measuring electrical resistivity of anisotropic materials: a revision of the montgomery method. *J. Appl Phys.* **110**, 083703 (2011).

Acknowledgements

This work was supported by the Arnold and Mabel Beckman Foundation via an AOB postdoctoral fellowship (https://doi.org/10.13039/100000997; awarded to G.S.). Materials supplies, and L.M.S. were supported by the Air Force Office for Scientific Research (AFOSR) under grant number FA9550-23-1-0635 (awarded to L.M.S.). M.J. and F.K. were supported by the National Science Foundation (NSF) through NSF grant OAC-2118310 (awarded to L.M.S.) and by the Princeton Center for Complex Materials, a National Science Foundation (NSF)-MRSEC program (DMR-2011750, awarded to L.M.S.). R.Y. was supported by JSPS KAKENHI Grant No. 22K20348, 23K13057, 24H01604 (awarded to R.Y.). We acknowledge support from the Japan Society for the Promotion of Science (JSPS) under Grant No. 23H05431 and 24H01607 (awarded to M.H.). This work was partially supported by the Japan Science and Technology Agency via JST CREST Grant Numbers JPMJCR1874, JPMJCR20T1 (Japan), and JST FOREST (JPMJFR2238, awarded to M.H.). Equipment used for this work was purchased using funds from the Gordon and Betty Moore Foundation's EPIQS initiative through Grants GBMF9064, The Packard Foundation, the Princeton Catalysis Initiative (PCI), and the Arnold and Mabel Beckman Foundation via a BYI grant to L.M.S. M.G.V. and I.R. acknowledge support to the Spanish Ministerio de Ciencia e Innovacion (grant PID2022-142008NB-I00, awarded to M.G.V.), partial support from European Research Council (ERC) grant agreement no. 101020833 (awarded to M.G.V.) and the European Union NextGenerationEU/PRTR-C17.I1 and the IKUR Strategy under the collaboration agreement between Ikerbasque Foundation and DIPC on behalf of the Department of Education of the Basque Government. M.G.V. acknowledges funding from the German Research Foundation (DFG) and the Austrian Science Fund (FOR 5249–QUAST, awarded to M.G.V.). M.G.V. and I.R. acknowledge funding supported by the Ministry of Economic Affairs and Digital Transformation of the Spanish Government through the QUANTUM ENIA project called—Quantum Spain project and by the European Union through the Recovery, Transformation, and Resilience Plan—NextGenerationEU within the framework of the Digital Spain 2026 Agenda. M.G.V. got support from the Canada Excellence Research Chairs Program for Topological Quantum Matter. FO and PM would like to acknowledge Dmitry Khalyavin for the fruitful discussion. The authors would like to thank the Science and Technology Facility Council (STFC-UKRI UK) for the provision of beam time on the WISH diffractometer.

Author contributions

G.S., M.H., and L.M.S. designed the research; G.S., F.O., I.R., M.J., R.Y., F.K., P.M. performed the experiments; G.S., F.O., I.R., P.M. analyzed the data; P.M., M.V., M.H., L.M.S. supervised the work; G.S., F.O., I.R., P.M., and L.M.S. wrote the initial draft. All authors edited the manuscript.

Competing interests

The authors declare no competing interests.

Additional information

Supplementary information The online version contains supplementary material available at https://doi.org/10.1038/s41467-024-54203-3.

Correspondence and requests for materials should be addressed to Leslie M. Schoop.

Peer review information *Nature Communications* thanks the anonymous, reviewer(s) for their contribution to the peer review of this work. A peer review file is available.